Published in final edited form as:
J Therm Sci Eng Appl. 2018 June ; 10(3): . doi:10.1115/1.4038763.

Effects of Femtosecond Laser Surface Processed Nanoparticle Layers on Pool Boiling Heat Transfer Performance

Corey Kruse,
Department of Mechanical and Materials Engineering, University of Nebraska–Lincoln, Lincoln, NE 68588

Mike Lucis,
Department of Mechanical and Materials Engineering, University of Nebraska–Lincoln, Lincoln, NE 68588

Jeff E. Shield,
Department of Mechanical and Materials Engineering, University of Nebraska–Lincoln, Lincoln, NE 68588

Troy Anderson,
Department of Electrical Engineering, University of Nebraska–Lincoln, Lincoln, NE 68588

Craig Zuhlke,
Department of Electrical Engineering, University of Nebraska–Lincoln, Lincoln, NE 68588

Dennis Alexander,
Department of Electrical Engineering, University of Nebraska–Lincoln, Lincoln, NE 68588

George Gogos, and
Department of Mechanical and Materials Engineering, University of Nebraska–Lincoln, Lincoln, NE 68588

Sidy Ndao
Department of Mechanical and Materials Engineering, University of Nebraska–Lincoln, Lincoln, NE 68588, sndao2@unl.edu

Abstract

An experimental investigation of the effects of layers of nanoparticles formed during femtosecond laser surface processing (FLSP) on pool boiling heat transfer performance has been conducted. Five different stainless steel 304 samples with slightly different surface features were fabricated through FLSP, and pool boiling heat transfer experiments were carried out to study the heat transfer characteristics of each surface. The experiments showed that the layer(s) of nanoparticles developed during the FLSP processes, which overlay FLSP self-organized microstructures, can either improve or degrade boiling heat transfer coefficients (HTC) depending on the overall thickness of the layer(s). This nanoparticle layer thickness is an indirect result of the type of microstructure created. The HTCs were found to decrease with increasing nanoparticle layer thickness. This trend has been attributed to added thermal resistance. Using a focused ion beam milling process and transmission electron microscopy (TEM), the physical and chemical properties of the nanoparticle layers were characterized and used to explain the observed heat

transfer results. Results suggest that there is an optimal nanoparticle layer thickness and material composition such that both the HTCs and critical heat flux (CHF) are enhanced.

Introduction

Two phase heat transfer, especially pool boiling, is a very attractive method for heat removal. With the general industry interest and demand for higher power density components, a very important limiting design parameter is heat dissipation. Two phase heat transfer has proven to produce very high heat transfer coefficients (HTC). Today, however, boiling heat transfer on conventional smooth surfaces is no longer able to accommodate the ever increasing cooling load required in emerging technologies. Physical and chemical functionalization of surfaces and various working fluids have recently been explored as ways to meet these high heat transfer demands. Such functionalizations have been shown to have a very significant effect on the boiling critical heat flux (CHF) as well as the HTC.

Recently, surface functionalization research has focused on the development of multiscale micro- and nanostructured surfaces for two-phase heat transfer enhancement. These types of surfaces are achieved through a wide variety of fabrication techniques. Using conventional microfabrication techniques, very organized structures, such as arrays of microposts and microchannels, can be fabricated. It has been demonstrated that such structures result in very good enhancements of the CHF as well as the HTC [1–4]. When nanoscale features are added to microscale structures, the boiling performance can be further enhanced. The addition of nanoscale features or particles can be accomplished in many ways. Typically, nanosize features consist of nanorods, nanowires, nanomaterial deposition, and nanoparticle thin film coatings [5,6]. The addition of these nanostructures has been shown to increase the wettability of the surface, increase nucleation site density, increase the available surface area, and promote capillary wicking. All of these factors aid in the improvement of boiling heat transfer and CHF. For example, the addition of nanowires to a surface can result in CHFs as high as 250 W/cm^2 [7–9] using de-ionized (DI) water as the working fluid, while the addition of copper nanorods has been demonstrated to result in a significant increase in the HTC but not in the CHF [10].

Porous micro/nanostructures have also recently gained much interest as a way to enhance pool boiling heat transfer. The general trend reported in the literature is that surfaces with high porosity promote capillary wicking and, therefore, result in higher CHFs due to more efficient cold liquid replenishment [11–13]. Porous structures on metallic surfaces can easily be achieved with a sintering process and have been shown to result in an enhancement of boiling heat transfer [14,15].

Improved pool boiling performance has also been achieved with the addition of only nanostructures or nanoparticle layers. Nanostructures are formed through a wide variety of techniques and can result in varying geometries from particles to complex nature-inspired shapes. There are contradicting results reported in the literature with respect to the effects of nanoscale modifications. It has been shown that the addition of nanoscale features can result in both increased CHF and HTC [16–18]. Using an electrochemical process to create nanostructures on a zircaloy surface, Ahn et al. [19] demonstrated a significant increase in

CHF but no major increase in HTC. On the other hand, Xu et al. [20], who also used an electrochemical process to create a nanostructured copper surface, saw an increase in CHF and HTC. Das and Bhaumik [21] deposited varying layers of titanium oxide on a copper heater surface and observed that the HTC increased greatly with an increase in film thickness; however, no real increase in CHF was observed. In the literature, it has been reported that nanoparticle layers can have adverse effects on the HTC of a surface [22–25]. Forrest et al. [22] deposited thin film coatings using a layer-by-layer technique and produced hydrophilic nickel and stainless steel surfaces which increased the CHF but greatly decreased the HTC. Seo et al. [23] deposited a nanolayer of carbon nanotubes onto a stainless steel surface and studied the boiling performance. They found that the CHF generally increased; but regardless of the layer thickness, the HTC decreased. Saeidi and Alemrajabi [24] using an electrochemical process, and Stutz et al. [25] using a coating process, each created nanoparticle layers of varied thickness on copper and platinum surfaces, respectively. Both sets of authors reported a general trend of increasing CHF along with either increasing or decreasing HTC depending on the nanoparticle layer thickness.

The use of nanofluids is another manufacturing method used to functionalize a surface through the addition of a nanoparticle layer. Typically, a specific nanofluid is boiled for a certain period of time and results in the deposition of a nanoparticle layer. This nanoparticle layer thickness generally increases with increased boiling time. In the literature, it has been reported that this nano-particle layer can impact boiling performance [26]. Experimental results reported in the literature show contradicting views on the effects of nanofluid functionalized surfaces with respect to HTC. The CHF is generally always increased, but the HTC is commonly much lower than a polished reference curve [27,28].

The development of functionalized surfaces is very important for the improvement of heat transfer systems. The use of multi-scale surfaces has been shown to significantly improve the boiling performance. However, the fundamental underlying mechanisms for this improvement are still not well understood. Femtosecond laser surface processing (FLSP) is another technique used to create multiscale functionalized metallic surfaces. This technique uses an ultrafast laser to create self-organized micro/nanostructures which can modify pool boiling heat transfer. In this paper, we focus on a new class of FLSP microstructures, nanoparticle covered pyramids (NC-pyramids) and show the importance of a nanoparticle layer that is developed during the FLSP process.

Pool Boiling Experimental Setup and Procedure

A pool boiling experimental setup was used for the heat transfer experiments. This experimental setup is shown in Fig. 1. The system was filled with 8 l of de-ionized water and maintained at atmospheric pressure. The system was brought to the saturation temperature of the liquid with the use of an immersion heater. The system was monitored for temperature and pressure using a combination of thermocouples and a pressure transducer. The water was degassed for about a half hour before testing was initiated. The vapor produced was directed through a coil condenser to maintain a constant system mass.

Once the system was allowed to reach the saturation temperature of the water, power to the heater was gradually increased using a copper heating block containing five cartridge heaters controlled with an analog variac. This copper heating block was attached to the upper copper heating block (see Fig. 1) with the use of a high temperature solder. The upper copper heating block has five thermocouple holes drilled to the center of the block. The thermocouples (located 3.18 mm apart) were used to measure the temperature gradient within the block in order to calculate the heat flux. The heat flux was calculated with a one-dimensional heat conduction equation based on the measured temperatures, known thermal conductivity, and the thermocouple spacing. Heat flux values were recorded after the system had reached steady-state, monitored through an in-house written LabVIEW program. The test section consists of a 25.4 mm diameter and 0.508 mm thick 304 stainless steel disk. The size of the test section was chosen to be sufficiently large in order to eliminate any effect of heater size on the CHF. The Bond number is used for correlating the heater size to its detrimental effects. The Bond number gives a ratio of heater size to bubble departure size. A test sample is considered to be sufficiently large if the Bond number is greater than three [29]. The Bond number was found to be around 100 for our specific experimental setup; thus, the heater size effect on the reported CHFs can be neglected.

The stainless steel test section thickness was chosen to minimize the operating temperatures of the heating block at high heat fluxes. The stainless steel test section was brazed onto the copper heating block using a silver brazing paste to ensure an efficient contact between the two materials. The surface temperature of the test section was calculated with a one-dimensional heat conduction equation using the average measured heat flux and the known thermal conductivities of the copper and stainless steel. The contact resistance between the copper and stainless steel was neglected due to the very thin and the highly conductive silver braze used. A high temperature PEEK plastic insulating bushing was used to insulate the upper copper heating block. Fiberglass insulation (not shown in Fig. 1) was used to insulate the lower copper heating block. High temperature silicon O-rings were used to seal between the concentric heating and insulating pieces. A special epoxy was used to ensure that nucleation would not prematurely occur on the outer edges of the boiling surface.

A complete description of the experimental errors in measuring the heat flux and surface temperature is described by Kruse et al. [30]. Using the standard propagation of errors equation, it was found that there was around a 7.5% experimental error in measuring the heat flux near the CHF and approximately 10% error in surface temperature measurements. It was assumed that the radial heat loss of the system was negligible and this was also verified by Kruse et al. [30] using theoretical analysis as well as finite element simulations.

Femtosecond Laser Surface Processing and Characterization

Femtosecond laser surface processing is a technique that uses a femtosecond laser to structure and functionalize metallic surfaces. These functionalized surfaces are characterized by a series of self-organized quasi-periodic microstructures covered by a layer of nanoparticles [31–34]. The geometry and physical characteristics of these formations depend on the laser fluence and number of incident pulses. These formations can be classified into three main classes: above surface growth mounds (ASG-mounds), below surface growth

mounds (BSG-mounds), and nanoparticle covered pyramids (NC-pyramids) [31–34]. Kruse et al. [35] showed that these formations exhibit extraordinary shifts of the Leidenfrost temperature, and in a separate study, BSG-mounds and ASG-mounds were studied for pool boiling performance [30]. In this study, the emphasis is on the effects of the unique nanoparticle layer of NC-pyramids on pool boiling performance.

A schematic of the FLSP setup is shown in Fig. 2. The fabrication laser was a Ti: Sapphire (Spitfire, Spectra Physics) femtosecond laser that produced ~80 fs pulses with a central wavelength of 800 nm at a 1 kHz repetition rate with a maximum pulse energy of 1 mJ. The laser power was controlled through the combination of a half-wave plate and a polarizer. The pulses were focused using a 152.4 mm focal parabolic mirror (MPD254762–90-P01). The sample was placed on a computer-controlled three-dimensional (3D) translation stage and translated, or rastered, through the beam path of the laser in order to process an area larger than the laser spot size. The number of pulses incident on the sample was controlled by adjusting the translation speed of the sample and the degree of overlap between raster scans.

Five samples were created with this laser processing technique that had various surface features. Four of these samples correspond to the NC-pyramid classification of microstructures. The fifth sample was fabricated with laser induced periodic surface structures (LIPSS) on the surface, a morphology with only nanoscale features and few nanoparticles. The surfaces were characterized with the use of a scanning electron microscope (SEM) and a laser scanning confocal microscope (Keyence VK-X210). The laser confocal microscope was used to obtain 3D surface profiles and measure geometric surface properties. The surface roughness, peak-to-valley height, and surface area ratio were calculated using output data from the laser confocal microscope. The visual difference between the samples and the characteristic surface dimensions and properties are shown in Fig. 3 and Table 1, respectively.

Nanoparticle covered pyramids are conical structures with an aspect ratio (between height and base diameter) of roughly one that are covered with a thick layer of nanoparticles. These structures have been described in detail by Zuhlke et al. [32]. The size and density of the NC-pyramids can be controlled by varying the pulse count and fluence of the ablation pulses during processing. NC-pyramids have base diameters and heights that range from 10 μm to 50 μm, but their size limits have not been quantified. NC-pyramids form at laser fluences near the ablation threshold of the 304 stainless steel with several thousand incident ablation pulses. NC-pyramids form through a combination of preferential valley ablation (PVA) and redeposition of nanoparticles created during the ablation process. PVA is a geometry-driven process in which laser light is reflected off of the angled sides of structures inducing a higher laser fluence and thus increased ablation in the valleys between structures. As the structures grow, the increased sub-tended area of the sidewalls reduces the fluence and amplifies this effect. The onset of NC-pyramid formation occurs at defect sites on the material surface, which have a higher ablation threshold than the surrounding material and serve as a scattering site starting the PVA process. The defect sites for the 304 stainless steel samples, prepared for this work, are likely from impurities that are either originally present in the material, develop as a result of the polishing process, or are created from the initial ablation pulses. The nanoparticle layer overlaying the NC-pyramids can be several microns thick and

builds up with each incident ablation pulse. During each raster pass, a layer of nanoparticles builds up on the surface of the NC-pyramids. The layer that develops during a single pass is sintered together as the laser passes over the pyramids, forming individual shells of nanoparticles. By placing a surface covered in NC-pyramids in an ultrasonic bath filled with de-ionized water, portions of nanoparticle shells become dislodged revealing the individual shells on the NC-pyramids. Examples of the individual shells of nanoparticles are visible in the SEM images of samples S3 and S4 in Fig. 3. The creation and redeposition of nanoparticles during FLSP of metals has been widely studied; however, the processes leading to nanoparticle production and redeposition are not fully understood [36,37].

Laser induced periodic surface structures resulting from FLSP is well published in the literature, including works on metals [38–40]. LIPSS do not contribute to the formation of the NC-pyramids; however, LIPSS are present over the entire ablation region at pulse counts before NC-pyramids begin to form, in the flat regions between NC-pyramids throughout the formation process, and even on the surface of the pyramids before the nanoparticle layer fully develops and covers the pyramids [32]. Processing with low pulse counts, before NC-pyramids start to develop, results in a surface covered in LIPSS without NC-pyramids. In this work, the LIPSS form perpendicular to the polarization of the incident pulses with a period just greater than 300 nm. The formation processes for LIPSS on metals is not fully understood, but current theories relate to nonuniform heating of the surface due to the interference of incident light with surface plasmons created from the early parts of the femtosecond pulses. The LIPSS structures develop as a result of a surface melt induced by the femtosecond pulses combined with the hydrodynamic effects associated with the nonuniform heating of the surface [38–41].

The contact angles were measured for each sample using a Rame-Hart model 590 F4 Series Goniometer and Tensiometer. The FLSP process inherently creates superhydrophilic surfaces. For samples S1–S4, the contact angles were considered to be near zero because of the superhydrophilic nature of the surface; droplets of de-ionized water wick extremely fast into the surface, and thus, a contact angle measurement cannot be obtained.

Samples S1 and S4 were created with different fluence and pulse count combinations in order to produce varied microstructure geometries. As can be seen by the images in Fig. 3, S4 consists of pyramid like structures arranged in a random pattern while S1 has pyramid structures that form microchannels (alternating ridges and valleys) with a separation of about 100 μm. Both of these samples were cleaned in an ultrasonic bath for 10 min after FLSP. The ultrasonic bath removes loose nanoparticles on the microstructures. Sample S1 was processed with a higher fluence and lower pulse count than S4, resulting in the formation of the microchannels.

Samples S2 and S3 were created with the same fluence and pulse count combination and were processed on the same day to ensure matching laser parameters. The goal of these two surfaces was to produce identical microstructure geometries and then use different post processing techniques to modify the nanoparticle layer. Sample S3 was given an ultrasonic bath in de-ionized water for 1 h after laser processing, while no postprocessing was completed for S2. The extended time in the ultrasonic bath significantly changed the

nanoparticle layer on the surface S3. This is evident when comparing the SEM images for S2 and S3 included in Fig. 3. For S3, the nanoparticle layer was fractured, resulting in layers and ridges on the sides of the microstructures. Finally, the LIPSS sample was created in order to study the effect of having only nanosized features on the surface.

Nanoparticle Layer Characterization

In order to gain understanding into the role that the nanoparticle layer present on the FLSP structures plays in pool boiling heat transfer enhancements, the nanoparticle layer was characterized on each of the FLSP pool boiling samples. In addition to the NC-pyramid surfaces, a BSG-mound and ASG-mound surface from a previous experiment were also characterized for comparison [30]. Samples used in the experiments were cross sectioned using a focused ion beam mill and then imaged using an SEM. This procedure allows for the physical measurement and imaging of the nanoparticle layers. All of the cross-sectional images were taken after the heat transfer data had been collected. In order to achieve an effective cross sectioning of a microstructure, a 100 nm thick carbon protective layer was first deposited with the use of the electron beam. An additional 10 μm of platinum was then deposited on the carbon layer to protect the nanoparticle layer from the subsequent ion beam milling process. After this deposition, an ion beam milling process was used to cross section an individual microstructure on each sample. The cross sections were then imaged with an SEM. This procedure was used to produce the images shown in Fig. 4.

As indicated by the arrows and corresponding labels in Fig. 4, there are three main regions of interest in each image. The top most-layer corresponds to the protective platinum layer. Beneath the platinum layer is the nanoparticle layer. It can be seen by inspection of the images that the nanoparticle layer varies greatly between the different samples. Beneath the nanoparticle layer is the solid core base material. In the S2 image, the rough features seen at the bottom of the core material is due to the ion beam milling process and not characteristic of the actual microstructure. The thickness of the nanoparticle layers for the various samples are summarized in Table 2. As expected, the NC-pyramid structures resulted in a significantly thicker nanoparticle layer compared to the mound structures. In the cases of S1 and S4, both of which went through a short ultrasonic bath (10 min), the nanoparticle layer varied from 2.4 to 2.5 μm and 1.1–5.0 μm, respectively. It should be noted that for S1, the cross sectioning was done along an entire ridge of pyramid structures visible in Fig. 3. As expected, due to the larger pulse count compared to S1 (see Table 1), the thickness of the nanoparticle layer in S2 is relatively larger, ranging from 3.7 to 4.7 μm. As for sample S3, which was produced under the same laser parameters as S2 but went through a long ultrasonic bath (1 h), the nanoparticle layer was found to be much more uneven with a layer thickness range from 0.9 to 2.2 μm. For comparison, the mound surfaces with heat transfer data included in Fig. 5 were also cross sectioned to measure the thickness of the nanoparticle layer. The nanoparticle layer for the mounds was found to be significantly smaller and was in the range of 0.3–0.9 μm for the BSG-mound samples and 0.2–0.6 μm for the ASG-mound sample.

In order to further characterize the nanoparticle layers, a transmission electron microscope (TEM) was used to study their material properties. Using a similar approach as previously

described, a thin section of a pyramid microstructure was milled out from sample S2. Using the TEM, it could be verified that the nanoparticle layer is indeed porous. We were also able to determine the material composition of the nanoparticles themselves. These results are shown in Fig. 6. The top image (imaged in bright mode) is taken at an interface between the protective platinum and carbon layer, the nanoparticle layer, and the bulk base material. The boundaries of the interfaces are indicated by the lines in Fig. 6. In this image, the vacancies correspond to the white areas. The bottom left image is a high angle annular dark field TEM image of the interface between the nanoparticle layer and the bulk material, where the black areas correspond to the vacancies in the nanoparticle layer. The bottom right image is an energy dispersion X-ray spectroscopy map taken at the same location as the bottom left image. This map gives the material composition of the sample.

From the TEM images it can be seen that the nanoparticle layer is indeed porous with white areas (bright field image) corresponding to vacancies in the material layer. Although the nanoparticle layer is porous it is quite dense with only nanosized pores. From the energy dispersion X-ray spectroscopy data, it was found that the nanoparticles created from the stainless steel surfaces are primarily composed of iron oxide and chromium oxide. This was determined by the ratio of the available elements. Although the data is not included here, it was also determined from the TEM analysis that these nanoparticles were crystalline in nature.

Results and Discussion

A boiling curve ranging from low heat flux up to the critical heat flux was generated for each of the five laser processed samples and the polished reference sample. The critical heat flux is reached when a nearly instantaneous increase in the surface temperature and simultaneous drop in the heat flux is observed. Results from the pool boiling experiments are shown in Fig. 5. The polished reference sample resulted in a CHF of 92 W/cm^2 at a superheat temperature of about 36°C. Each of the processed samples resulted in an increase in the CHF. The NC-pyramid structures (S1–S4) all resulted in similar CHFs. The largest measured CHF was 141 W/cm^2, corresponding to sample S2. Sample S4 resulted in the lowest CHF for the pyramid samples with a value of 123 W/cm^2. The LIPSS sample resulted in some enhancement of the CHF with respect to the polished sample with a CHF of 101 W/cm^2.

Also shown in Fig. 5 are two boiling curves corresponding to BSG-mound and ASG-mound samples reported previously [30]. BSG and ASG-mounds are created using a higher fluence and lower pulse count combination in comparison to NC-pyramids [30]. This combination of laser parameters results in a higher aspect ratio as well as a less pronounced nanoparticle layer than NC-pyramids as previously shown. Initial thoughts were that FLSP NC-pyramid surfaces might result in the highest enhancement of the boiling HTCs due to the presence of a thicker nanoparticle layer, resulting in more available surface area. In our previous study on the Leidenfrost temperature of FLSP surfaces [35], we found that an increase in porosity, due to a thicker nanoparticle layer, resulted in the highest increase of the Leidenfrost temperature for NC-pyramid surfaces compared to that of BSG and ASG-mounds. The present study shows that, in comparison to the BSG and ASG-mounds, the NC-pyramid

structures have nearly the same CHFs but overall much lower HTCs. Admittedly, the enhancement of the CHF results from a multimechanistic contribution of various factors which include an increase in wettability, capillary wicking, roughness, and surface area, and thus, trends cannot easily be attributed to one specific parameter. The fact that the CHF of the pyramid surfaces is nearly identical to the mound structures leads us to believe that the significant change in nanoparticle layer does not have any significant impact on the critical heat flux. On the other hand, it is quite evident that the nanoparticle layer does have a very significant impact on the HTC, as evident from the data included in Fig. 5.

A unique trend in the boiling curve of the FLSP surfaces is also observed in Fig. 5. An increase in the HTC near the CHF is observed, resulting in a “hook back” of the curve. This hook back is referred to as secondary boiling effects and is attributed to the unique characteristics of the FLSP surfaces. A further explanation of secondary boiling effects is given by Kruse et al. [42].

In Fig. 5, all of the pyramid surfaces except S3 result in a decrease in HTC relative to the polished reference curve. A decrease in HTC is represented as a shift to the right of the boiling curve relative to the polished sample. The HTC is calculated as the heat flux divided by the wall superheat temperature. Samples S1, S2, and S4 all have significantly increased surface roughness and surface area over the polished sample which, based on the literature, should result in an increase in HTC [6]. Contrary to the literature, this was not seen. This leads us to believe that something is overcoming the positive benefits of increased surface area and roughness and reducing the overall performance. The HTC for S2 was the lowest out of all surfaces and corresponded to the largest and most uniform nanoparticle layer. As the nanoparticle layer thickness and uniformity were decreased (see Fig. 4), the HTC increased (S1 and S4) relative to S2 but was still lower than the polished sample. S3 underwent an aggressive nanoparticle removal through a long ultrasonic bath and resulted in the highest HTC of all the NC-pyramid surfaces, even outperforming the polished reference. Although it outperformed the polished sample, it produced HTCs significantly lower than the ASG and BSG mound structures. It can clearly be seen that the nanoparticle layer plays a large role in the heat transfer coefficient and as the nanoparticle layer thickness and uniformity increases, the HTC decreases.

To separate the effects of microversus nanoscale features on the heat transfer performance, we investigated the LIPSS sample. Nanoscale features on the LIPSS sample are formed directly into the surface material unlike the redeposition mechanism described previously in the case of the NC-pyramid samples and thus are not made up of nanoparticles. This produces nanoscale features without microstructures. The data in Fig. 5 show that the LIPSS sample resulted in a higher HTC than S1, S2, and S4 and a similar HTC to S3. This is important because it illustrates the effect of the nanoparticle layer that is present in the NC-pyramid surfaces. The NC-pyramid surfaces have surface area ratios much larger and surface roughness nearly two orders of magnitude greater than the LIPSS surface, yet the LIPSS surface results in higher HTC values than S1, S2, and S4 and nearly identical values to S3. The ASG and BSG samples also contribute to this theory. The ASG and BSG surfaces both have very thin nanoparticle layers compared to the NC-pyramid surfaces but do have comparable roughness, microstructure heights, and surface area ratios. Both of these

surfaces resulted in drastically higher HTC values, which again lead to the effect of the nanoparticle layer.

Through analysis of the results in Fig. 5 it is concluded that the thickness of a nanoparticle layer on surfaces with microscale roughness can have either a positive or negative effect on the HTC. The same conclusion has also been reported in the literature [23–25]. The current understanding in the literature for the degradation of the two-phase HTCs as a result of increased nanoparticle thickness is twofold. First, the nanoparticle layer can act as a thermal insulator due to the oxide composition of the nanoparticles. Second, it can actually result in a decrease in the surface roughness and a smaller average nucleation site [43]. The first understanding is easily supported by the previously described surfaces. The nanoparticle layer that covers the FLSP microstructures is composed of iron oxide and chromium oxide which have a lower thermal conductivity than the bulk material, thus providing insulation. The thicker the layer, the greater the insulating effect. The second understanding is typically seen on surfaces where the nanoparticles are much smaller the original cavity sizes on a surface. It is argued that, as the nanoparticle layer builds up, it can fill in and smooth out previously present surface features, thus reducing the surface roughness. This mechanism is not dominant in the FLSP surfaces of this study since additional microstructures are present that provide an abundance of potential nucleation cavities, however, the theory is still relevant. As seen on the far-most right column of Fig. 3, samples S2 and S3 have significantly different surface roughness on the sides of the microstructures. Sample S3 has a higher quantity of larger cavities because of the cracked nanoparticle layers. This results in a wider size range of potential nucleation cavities as well as a reduction in the overall thickness of the insulating layer, both of which lead to increased HTC (see Fig. 5). Based on these results and knowledge available in the open literature, two-phase enhancement from multiscale structured surfaces in the nucleate boiling regime is believed to be governed by: increased heat transfer surface area, capillary wicking, ranging potential nucleation cavity sizes, effective thermal conductivity across aggregated nanoparticles, and escaping vapor efficiency. A schematic drawing of all these mechanisms at play is shown in Fig. 7.

As illustrated in Fig. 7, nanoparticles or nanoscale features are represented as a porous layer that induces capillary wicking but also introduces additional thermal resistances (i.e., insulating effect) due to weak physical and thermal contact between nanoparticles and an oxide layer encapsulating each individual nanoparticle. In competition with increased thermal resistance are more efficient capillary wicking actions and increased surface area, both of which have opposite effects on the two-phase thermal performance. The porous layer promotes capillary wicking which leads to increased heat transfer performance. Evaporation bubble dynamics play an important role in the boiling process but can be impeded with the addition of a nanoparticle layer that is too thick and less penetrable by the working fluid. Nucleation that occurs inside the porous layer must grow and travel through the porous layer. The suppression of this dynamic can lead to a premature CHF and counteracts capillary wicking actions. Both of these have the effects of reducing the HTCs and CHF. The proposed mechanisms illustrated in Fig. 7 demonstrate that the addition of nanoparticle layers can have both positive and negative effects on heat transfer performance.

In the case of the NC-pyramid surfaces, a porous nanoparticle layer is present and depicted in Fig. 6. It can be observed from the results shown in Fig. 6 that the nanoparticles are densely packed and result in very small nanosized pores. For this nanoparticle layer to be beneficial, it must promote capillary wicking which is well known to increase CHF. It is unlikely that this nanoparticle layer promotes wicking due to the very small pores and surface tension of the water. It is more likely that the pores are filled with air during the formation process. The addition of air into the surface will increase the thermal resistance of the nanoparticle layer. In addition to this, the nanoparticles themselves are not well connected to each other as evident by the ultrasonic bath process. This produces a contact resistance between particles. The nanoparticles are also made up of metal oxides which have a lower thermal conductivity than the base material. The oxides also result in an increase in the insulation effect of the nanoparticle layer. Nucleation is unlikely in the nanoparticle layer due to the very small pore sizes and dense nature. In a previous study the active nucleation cavity sizes were estimated using available models and it was found that based on the superheat temperature and contact angle of the surface, a minimum cavity size of about 1.5 μm at the onset of nucleation could be active and a cavity size of about 0.5 μm could be active with a wall superheat temperature of about 25 deg [42]. This is still much larger than any cavity seen in the nanoparticle layer and thus illustrates an additional negative effect of the nanoparticle layer. Any vapor that could be generated in the nanoparticle layer cannot escape easily due to the dense nature, which based on the proposed mechanism will also lead to a degradation of heat transfer performance. This explains why there is no significant increase in critical heat flux when the nanoparticle layer thickness is increased. In the case of sample S3, these insulating effects are reduced when the nanoparticle layer is partially removed (compared to S2).

For the given NC-pyramid surfaces, the nanoparticle layer is not generally beneficial because it acts to suppress nucleation, does not adequately promote capillary wicking, and effectively insulates the boiling surface. Through this experiment, it has been found that the insulating effects of the nanoparticle layer on two-phase heat transfer performance can dominate all the other positive attributes, such as increased surface area, capillary wicking, and increased surface roughness. One of the primary goals of the described experiment is to highlight the importance of understanding the microstructure features below the surface in order to fully understand the governing mechanisms for pool boiling with highly modified surfaces. As shown by this work, unexpected negative results were fully understood and explained after cross section images were obtained and the true features of the layer affecting heat transfer was exposed.

One common concern with the nanoparticle layer is whether or not it is removed during the boiling process. To address this concern, SEM images were taken before and after the boiling heat transfer experiments. These images are shown in Fig. 8. No change is visible in the nanoparticle layers before and after boiling. It is therefore concluded that the cross-sectional images taken after the heat transfer experiments are true representations of the surface nanoparticle layer prior to boiling.

Conclusions

In this study, experiments were conducted on five different 304 stainless steel FLSP surfaces with an emphasis of the work to understand the role of nanoparticle layers on the two-phase heat transfer performance. The surfaces studied fit into a class of structures termed nanoparticle covered pyramids or NC-pyramids. These NC-pyramid structures were evaluated for pool boiling performance and compared to previously studied BSG and ASG-mound structures. Unexpected and negative heat transfer performance results (decrease in HTC) were obtained with most of the NC-pyramid surfaces. Following the pool boiling studies the surfaces were cross sectioned to physically measure and characterize the nanoparticle layers. It was found that the thickness of the nanoparticle layers has a significant impact on the HTC and CHF of a surface. In general, the NC-pyramid surfaces performed worse than the polished reference surface in terms of HTCs except for one which had the nanoparticle layer on the NC-pyramids significantly removed following FLSP. Overall, the HTCs were found to decrease with increasing nanoparticle layer thickness while no significant trend was observed with the CHF. This trend in HTC has been attributed to the added thermal resistance of the nanoparticle layer due to entrapped air, contact resistances between particles, and lower thermal conductivity of nanoparticles due to the presence of oxides. Governing mechanisms have been proposed to explain the observed results. It is believed that nanoparticle layers can have both a positive and negative effect on the heat transfer performance depending on their thickness, porosity, and material composition. This experiment highlights the importance of studying the microstructure features below the visible surface to fully understand the heat transfer results. It is also expected that there must be an optimal nanoparticle layer thickness and material composition such that both the HTC and CHF are enhanced.

Acknowledgments

Funding Data

- NASA Space Technology Research Fellowship (Grant No.NNX14AM50H).
- National Science Foundation (Award No. ECCS: 1542182).
- Nebraska Center for Energy Sciences Research, University of Nebraska-Lincoln (Grant Nos. A-00-A-03 and 803).
- Office of Experimental Program to Stimulate Competitive Research (Grant No. 2014–198-SC1).
- Office of Naval Research Global (Grant No. FA4600–12-D-9000–00).

References

[1]. Ndao S, Peles Y, and Jensen MK, 2012, “Experimental Investigation of Flow Boiling Heat Transfer of Jet Impingement on Smooth and Micro Structured Surfaces,” Int. J. Heat Mass Transfer, 55(19–20), pp. 5093–5101.

[2]. Kim S, Kim HD, Kim H, Ahn HS, Jo H, Kim J, and Kim MH, 2010, “Effects of Nano-Fluid and Surfaces With Nano Structure on the Increase of CHF,” Exp. Therm. Fluid Sci, 34(4), pp. 487–495.

[3]. Chu K-H, Enright R, and Wang EN, 2012, “Structured Surfaces for Enhanced Pool Boiling Heat Transfer,” Appl. Phys. Lett, 100(24), p. 241603.

[4]. Yao Z, Lu Y-W, and Kandlikar SG, 2012, "Micro/Nano Hierarchical Structure in Microchannel Heat Sink for Boiling Enhancement," IEEE 25th International Conference Micro Electro Mechanical Systems (MEMS), Paris, France, Jan. 29–Feb 2, pp. 285–288.

[5]. Bang I-C, and Jeong J-H, 2011, "Nanotechnology for Advanced Nuclear Thermal-Hydraulics and Safety: Boiling and Condensation," Nucl. Eng. Technol, 43(3), pp. 217–242.

[6]. Lu Y, and Kandlikar S, 2011, "Nanoscale Surface Modification Techniques for Pool Boiling Enhancement—A Critical Review and Future Directions," Heat Transf. Eng, 32(10), pp. 827–842.

[7]. Chen R, Lu M-C, Srinivasan V, Wang Z, Cho HH, and Majumdar A, 2009, "Nanowires for Enhanced Boiling Heat Transfer," Nano Lett, 9(2), pp. 548–553. [PubMed: 19152275]

[8]. Lu M-C, Chen R, Srinivasan V, Carey VP, and Majumdar A, 2011, "Critical Heat Flux of Pool Boiling on Si Nanowire Array-Coated Surfaces," Int. J. Heat Mass Transfer, 54(25–26), pp. 5359–5367.

[9]. Yao Z, Lu Y-W, and Kandlikar SG, 2011, "Effects of Nanowire Height on Pool Boiling Performance of Water on Silicon Chips," Int. J. Therm. Sci, 50(11), pp. 2084–2090.

[10]. Li C, Wang Z, Wang P-I, Peles Y, Koratkar N, and Peterson GP, 2008, "Nanostructured Copper Interfaces for Enhanced Boiling," Small, 4(8), p. 1084. [PubMed: 18570277]

[11]. Patil CM, and Kandlikar SG, 2014, "Review of the Manufacturing Techniques for Porous Surfaces Used in Enhanced Pool Boiling," Heat Transfer Eng, 35(10), pp. 887–902.

[12]. Liter SG, and Kaviany M, 2001, "Pool-Boiling CHF Enhancement by Modulated Porous-Layer Coating: Theory and Experiment," Int. J. Heat Mass Transfer, 44(22), pp. 4287–4311.

[13]. Rahman M, Olçeroğlu E, and McCarthy M, 2014, "Role of Wickability on the Critical Heat Flux of Structured Superhydrophilic Surfaces," Langmuir, 30(37), pp. 11225–11234. [PubMed: 25171197]

[14]. McHale JP, Garimella SV, Fisher TS, and Powell GA, 2011, "Pool Boiling Performance Comparison of Smooth and Sintered Copper Surfaces With and Without Carbon Nanotubes," Nanoscale Microscale Thermophys. Eng, 15(3), pp. 133–150.

[15]. Li C, and Peterson GP, 2007, "Parametric Study of Pool Boiling on Horizontal Highly Conductive Microporous Coated Surfaces," ASME J. Heat Transfer, 129(11), pp. 1465–1475.

[16]. Hendricks TJ, Krishnan S, Choi C, Chang C-H, and Paul B, 2010, "Enhancement of Pool-Boiling Heat Transfer Using Nanostructured Surfaces on Aluminum and Copper," Int. J. Heat Mass Transfer, 53(15–16), pp. 3357–3365.

[17]. Im Y, Dietz C, Lee SS, and Joshi Y, 2012, "Flower-Like CuO Nanostructures for Enhanced Boiling," Nanoscale Microscale Thermophys. Eng, 16(3), pp. 145–153.

[18]. Launay S, Fedorov AG, Joshi Y, Cao A, and Ajayan PM, 2006, "Hybrid Micro-Nano Structured Thermal Interfaces for Pool Boiling Heat Transfer Enhancement," Microelectron. J, 37(11), pp. 1158–1164.

[19]. Ahn HS, Lee C, Kim H, Jo H, Kang S, Kim J, Shin J, and Kim MH, 2010, "Pool Boiling CHF Enhancement by Micro/Nanoscale Modification of Zircaloy-4 Surface," Nucl. Eng. Des, 240(10), pp. 3350–3360.

[20]. Xu P, Li Q, and Xuan Y, 2015, "Enhanced Boiling Heat Transfer on Composite Porous Surface," Int. J. Heat Mass Transfer, 80, pp. 107–114.

[21]. Das S, and Bhaumik S, 2014, "Enhancement of Nucleate Pool Boiling Heat Transfer on Titanium Oxide Thin Film Surface," Arab. J. Sci. Eng, 39(10), pp. 7385–7395.

[22]. Forrest E, Williamson E, Buongiorno J, Hu L-W, Rubner M, and Cohen R, 2010, "Augmentation of Nucleate Boiling Heat Transfer and Critical Heat Flux Using Nanoparticle Thin-Film Coatings," Int. J. Heat Mass Transfer, 53(1–3), pp. 58–67.

[23]. Seo GH, Hwang H, Yoon J, Yeo T, Son HH, Jeong U, Jeun G, Choi W, and Kim SJ, 2015, "Enhanced Critical Heat Flux With Single-Walled Carbon Nanotubes Bonded on Metal Surfaces," Exp. Therm. Fluid Sci, 60, pp. 138–147.

[24]. Saeidi D, and Alemrajabi AA, 2013, "Experimental Investigation of Pool Boiling Heat Transfer and Critical Heat Flux of Nanostructured Surfaces," Int. J. Heat Mass Transfer, 60, pp. 440–449.

[25]. Stutz B, Morceli CHS, da Silva MDF, Cioulachtjian S, and Bonjour J, 2011, "Influence of Nanoparticle Surface Coating on Pool Boiling," Exp. Therm. Fluid Sci, 35(7), pp. 1239–1249.

[26]. Seon Ahn H, and Hwan Kim M, 2012, "A Review on Critical Heat Flux Enhancement With Nanofluids and Surface Modification," ASME J. Heat Transfer, 134(2), p. 024001.

[27]. Sheikhbahai M, Nasr Esfahany M, and Etesami N, 2012, "Experimental Investigation of Pool Boiling of Fe_3O_4/Ethylene Glycol–Water Nanofluid in Electric Field," Int. J. Therm. Sci, 62, pp. 149–153.

[28]. Shahmoradi Z, Etesami N, and Nasr Esfahany M, 2013, "Pool Boiling Characteristics of Nanofluid on Flat Plate Based on Heater Surface Analysis," Int. Commun. Heat Mass Transfer, 47, pp. 113–120.

[29]. Kim J, Benton JF, and Wisniewski D, 2002, "Pool Boiling Heat Transfer on Small Heaters: Effect of Gravity and Subcooling," Int. J. Heat Mass Transfer, 45(19), pp. 3919–3932.

[30]. Kruse CM, Anderson T, Wilson C, Zuhlke C, Alexander D, Gogos G, and Ndao S, 2015, "Enhanced Pool-Boiling Heat Transfer and Critical Heat Flux on Femtosecond Laser Processed Stainless Steel Surfaces," Int. J. Heat Mass Transfer, 82, pp. 109–116.

[31]. Zuhlke C, Anderson T, and Alexander D, 2013, "Formation of Multiscale Surface Structures on Nickel Via Above Surface Growth and Below Surface Growth Mechanisms Using Femtosecond Laser Pulses," Opt. Express, 21(7), pp. 8460–8473. [PubMed: 23571936]

[32]. Zuhlke CA, Anderson TP, and Alexander DR, 2013, "Fundamentals of Layered Nanoparticle Covered Pyramidal Structures Formed on Nickel During Femtosecond Laser Surface Interactions," Appl. Surf. Sci, 283, pp. 648–653.

[33]. Zuhlke CA, Anderson TP, and Alexander DR, 2013, "Comparison of the Structural and Chemical Composition of Two Unique Micro/Nanostructures Produced by Femtosecond Laser Interactions on Nickel," Appl. Phys. Lett, 103(12), p. 121603.

[34]. Zuhlke CA, Alexander DR, Bruce JC, Ianno NJ, Kamler CA, and Yang W, 2010, "Self Assembled Nanoparticle Aggregates From Line Focused Femtosecond Laser Ablation," Opt. Express, 18(5), pp. 4329–4339. [PubMed: 20389444]

[35]. Kruse C, Anderson T, Wilson C, Zuhlke C, Alexander D, Gogos G, and Ndao S, 2013, "Extraordinary Shifts of the Leidenfrost Temperature From Multiscale Micro/Nanostructured Surfaces," Langmuir, 29(31), pp. 9798–9806. [PubMed: 23799305]

[36]. Eliezer S, Eliaz N, Grossman E, Fisher D, Gouzman I, Henis Z, Pecker S, Horovitz Y, Fraenkel M, Maman S, and Lereah Y, 2004, "Synthesis of Nanoparticles With Femtosecond Laser Pulses," Phys. Rev. B, 69(14), p. 144119.

[37]. Vorobyev AY, and Guo C, 2006, "Back Deposition of Ablated Particles Onto Sample in Femtosecond Laser Processing of Metals," IEEE Eighth International Conference on Laser Fiber-Optical Networks Model (LFNM), Kharkiv, Ukraine, June 29–July 1, pp. 39–41.

[38]. Okamuro K, Hashida M, Miyasaka Y, Ikuta Y, Tokita S, and Sakabe S, 2010, "Laser Fluence Dependence of Periodic Grating Structures Formed on Metal Surfaces Under Femtosecond Laser Pulse Irradiation," Phys. Rev. B, 82(16), p. 165417.

[39]. Vorobyev AY, Makin VS, and Guo C, 2007, "Periodic Ordering of Random Surface Nanostructures Induced by Femtosecond Laser Pulses on Metals," J. Appl. Phys, 101(3), p. 034903.

[40]. Sakabe S, Hashida M, Tokita S, Namba S, and Okamuro K, 2009, "Mechanism for Self-Formation of Periodic Grating Structures on a Metal Surface by a Femtosecond Laser Pulse," Phys. Rev. B, 79(3), p. 033409.

[41]. Tsibidis GD, Barberoglou M, Loukakos PA, Stratakis E, and Fotakis C, 2012, "Dynamics of Ripple Formation on Silicon Surfaces by Ultrashort Laser Pulses in Subablation Conditions," Phys. Rev. B, 86(11), p. 115316.

[42]. Kruse C, Tsubaki A, Zuhlke C, Anderson T, Alexander D, Gogos G, and Ndao S, 2016, "Secondary Pool Boiling Effects," Appl. Phys. Lett, 108(5), p. 051602.

[43]. Vafaei S, and Borca-Tasciuc T, 2014, "Role of Nanoparticles on Nanofluid Boiling Phenomenon: Nanoparticle Deposition," Chem. Eng. Res. Des, 92(5), pp. 842–856.

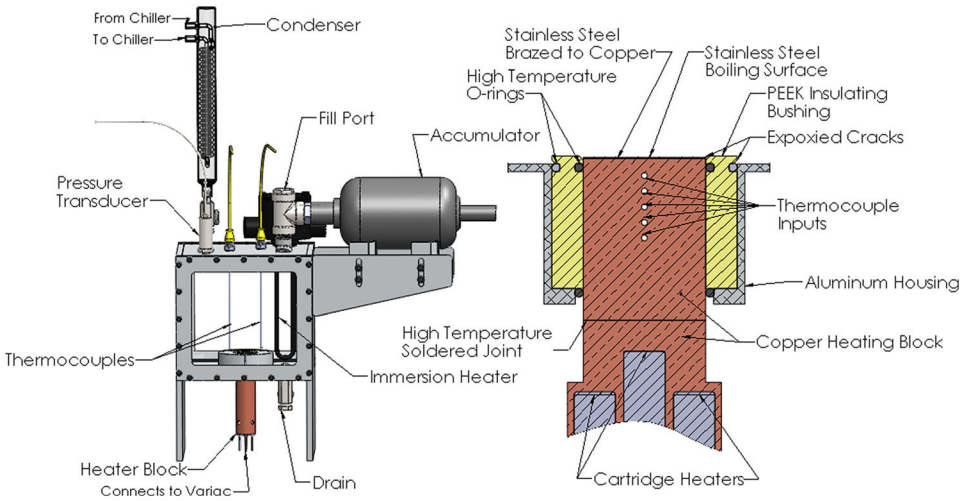

Fig. 1.

Left: pool boiling setup and right: cross-sectional view of heating block and boiling surface

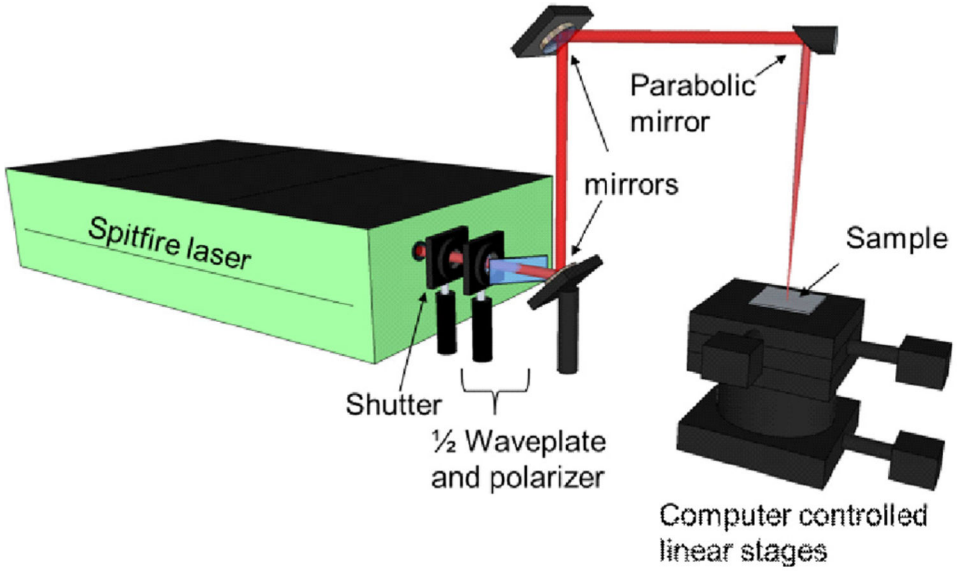

Fig. 2.
Schematic for FLSP

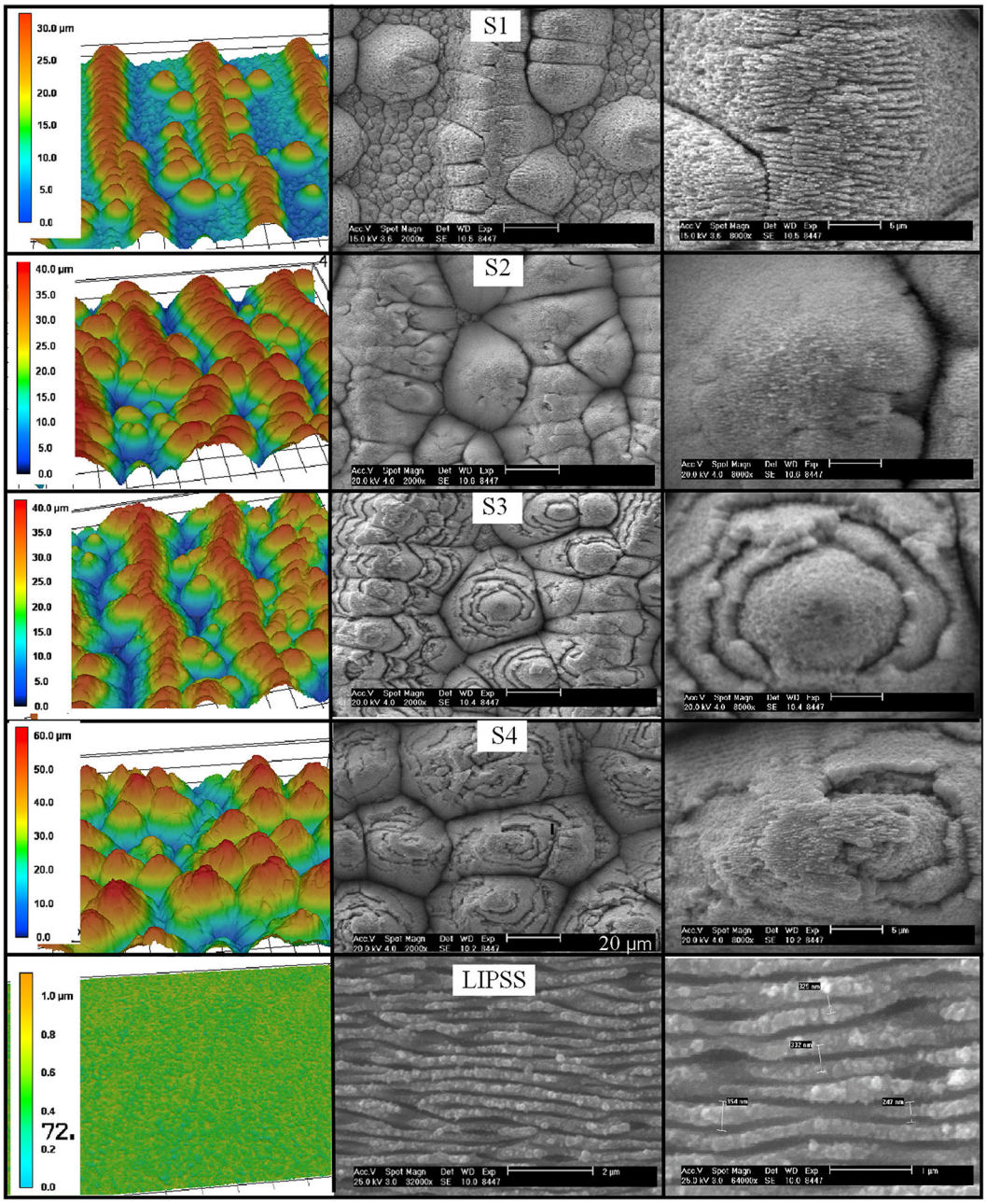

Fig. 3.

Left: laser confocal 3D images, middle: SEM images (S1–S4 20 μm scale bar, LIPSS 2 μm scale bar), and right: SEM images (S1–S4 5 μm scale bar, LIPSS 1 lm scale bar)

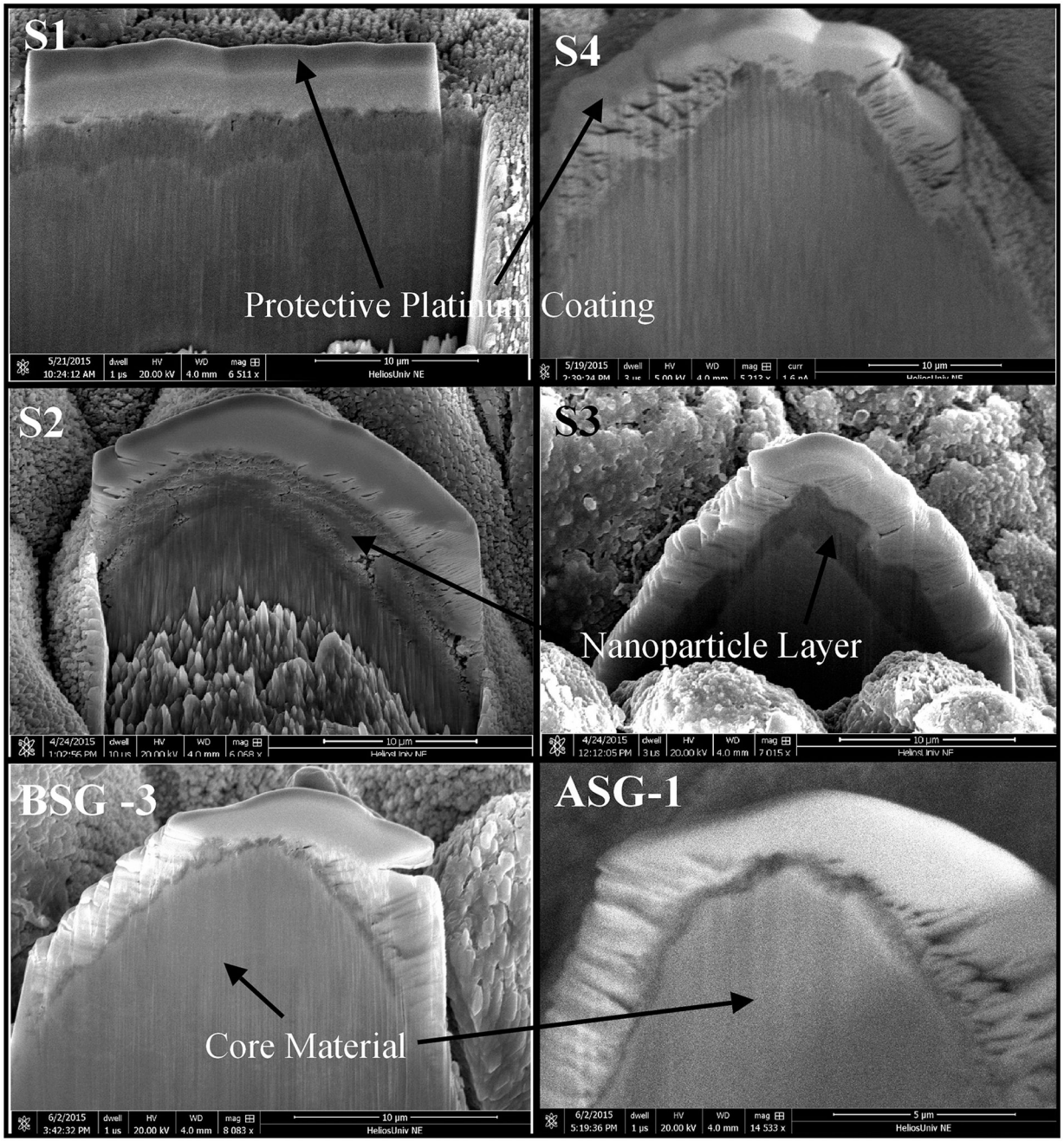

Fig. 4.

Images of cross sections for each of the samples in Fig. 3. In each image the white top layer corresponds to the platinum layer. Beneath the platinum is the nanoparticle layer (dark gray) and below the nanoparticle layer is the core material (light gray). Scale bars are 10 μm for all surfaces except ASG-1 which is 5 μm.

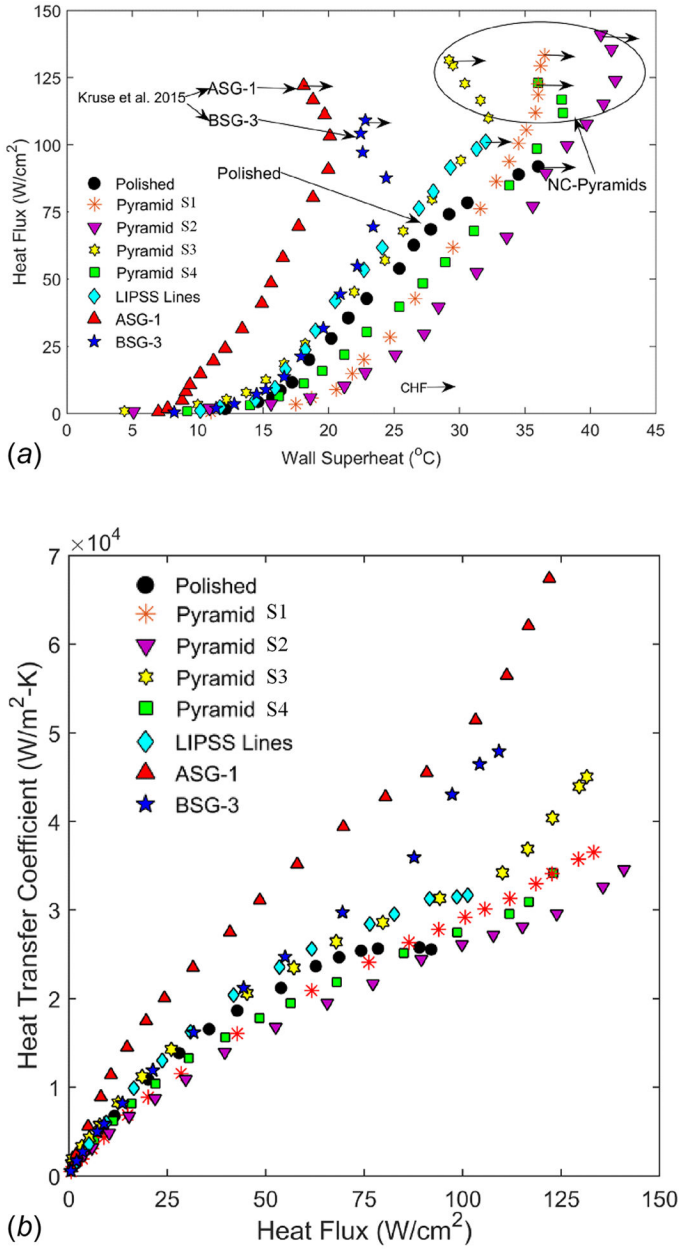

Fig. 5.

Top: pool boiling curves for the NC-pyramid structures as well as the LIPSS surface and previously published ASG and BSG-Mound structures. Bottom: HTCs with respect to heat flux for the same surfaces.

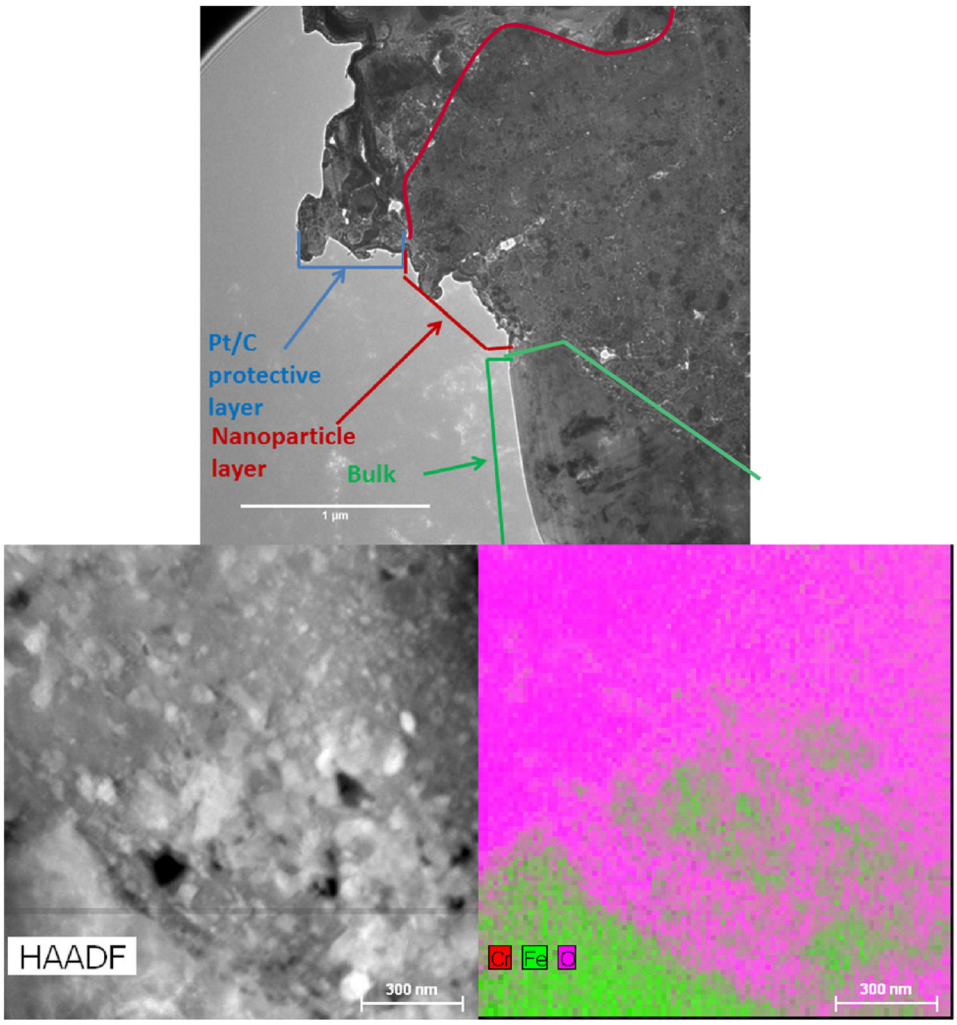

Fig. 6.

Top: cross section view of the nanoparticle layer and bulk material interface (1 μm scale bar). Bottom left: high angle annular dark field TEM image of the interface between the nanoparticle layer and the bulk material. Bottom right: combined energy dispersion X-ray spectroscopy map of the interface showing that the nanoparticles are primarily composed of iron, chromium, and oxygen (300 nm scale bar).

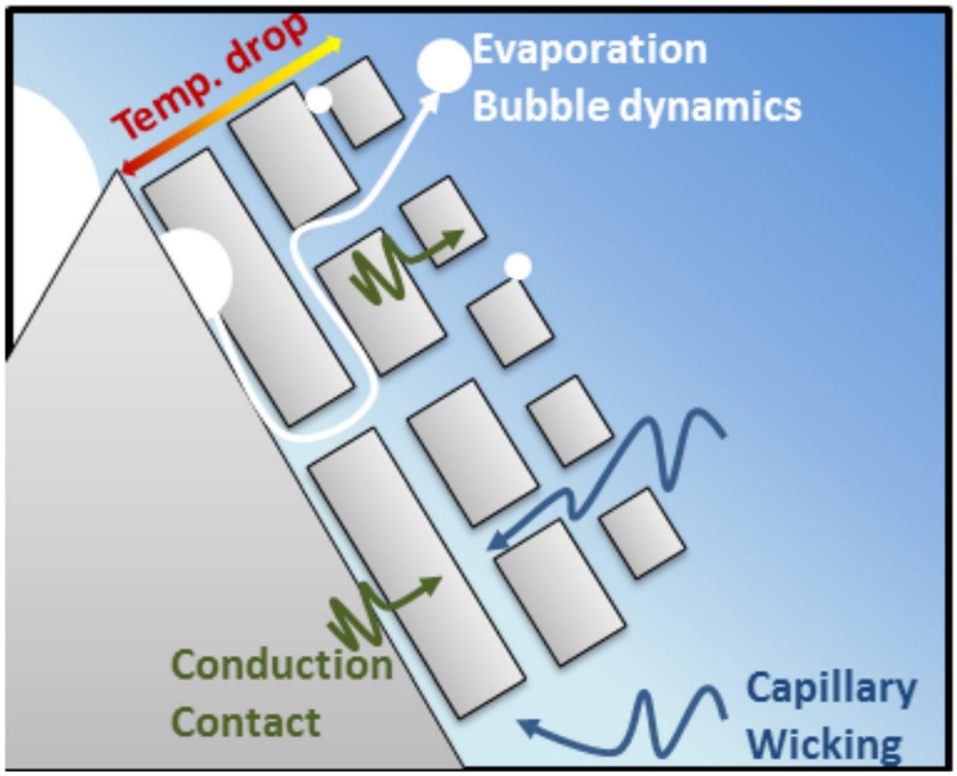

Fig. 7.

Schematic describing the balancing mechanism among evaporation dynamics, conduction heat transfer, and liquid supply due to capillary wicking

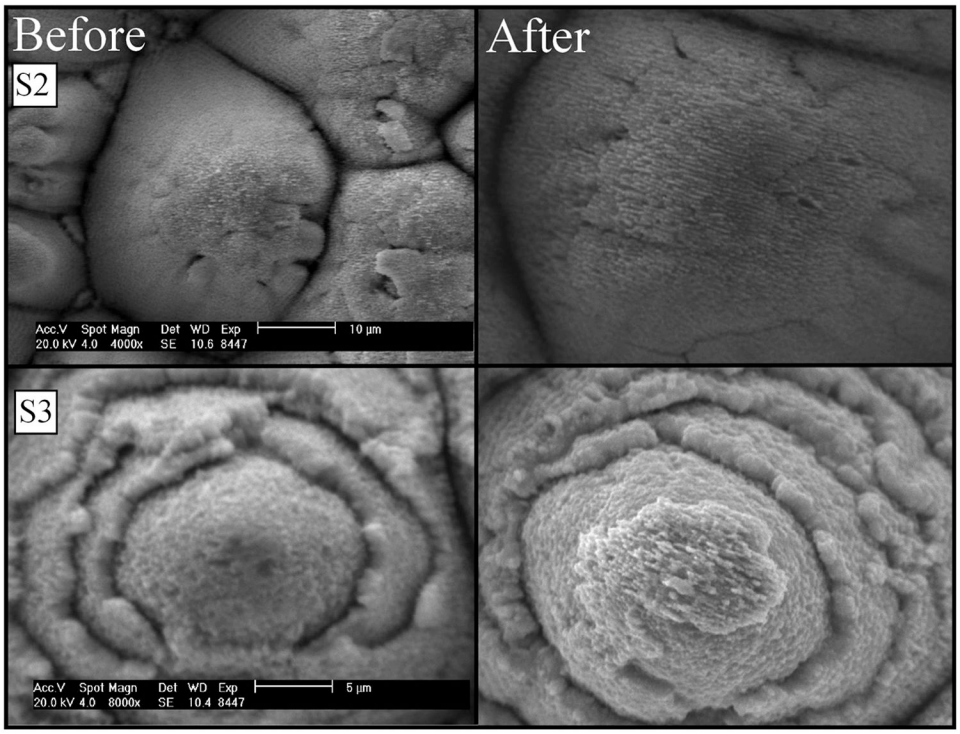

Fig. 8.
Left: S2 and S3 before testing and right: S2 and S3 after testing

Table 1

Physical characteristics of polished and laser processed surfaces

Sample	Peak fluence (J/cm^2)	Pulse count	Peak-to-valley height (μm)	Surface roughness (μm)	Surface area ratio	Contact angle (deg)	Ultrasonic bath time (min)
Polished	—	—	—	0.2	1.1	80	0
Pyramid, S1	0.39	2997	25.8	8.2	2.7	0	10
Pyramid, S2	0.37	6518	35.5	9.6	3.0	0	0
Pyramid, S3	0.37	6518	33.5	9.2	3.2	0	60
Pyramid, S4	0.29	17,034	47.2	11.8	3.6	0	10
LIPSS	0.39	86	0.9	0.2	1.6	65	0

Table 2

Measured nanoparticle thickness for each of the tested FLSP surfaces

Sample	Pyramid S1	Pyramid S2	Pyramid S3	Pyramid S4	BSG-3	ASG-1
Nanoparticle thickness range (μm)	2.4–2.5	3.7–4.7	0.9–2.2	1.1–5.0	0.3–0.9	0.2–0.6